Proceedings of the 11th Brazilian Congress of Thermal Sciences and Engineering – ENCIT 2006
Braz. Soc. of Mechanical Sciences and Engineering – ABCM, Curitiba, Brazil, Dec. 5-8, 2006

Paper CIT06-1074

ON THE VORTEX PAIRING AEROACOUSTICS OF A 2D MIXING LAYER UNDER TEMPORAL DEVELOPMENT

Alysson Kennerly Colaciti
USP - Universidade de São Paulo, NPA - SMM - EESC. Av. Trabalhador Sãocarlense, 400, Centro, cep:13560-970, São Carlos - SP Brasil
alyssonkennerly@gmail.com

Ricardo A. Coppola Germanos
University of Arizona / USP - Universidade de São Paulo, NPA - SMM - EESC. Av. Trabalhador Sãocarlense, 400, Centro, cep:13560-970, São Carlos - SP Brasil
gercop@sc.usp.br

Marcello Augusto Faraco de Medeiros
USP - Universidade de São Paulo, NPA - SMM - EESC. Av. Trabalhador Sãocarlense, 400, Centro, cep:13560-970, São Carlos - SP Brasil
marcello@sc.usp.br

Abstract. *The aim of the present work is to investigate numerically the aeroacoustics of a vortex pairing in the temporal development of a free shear layer. Direct numerical simulation with high accuracy finite difference scheme was employed in this research. A characteristic-type formulation of the compressible 2D Navier Stokes equations was used. One of the main challenges found on the development of this research was to produce a single vortex pairing in the middle of a wide computational domain. Time development of mixing layers adopts the periodic boundary condition in x-direction, what makes it more difficult to reproduce a single vortex pairing inside a wide domain. The domain must be large enough to provide a clear observation of the acoustic field produced by the pairing. The simulation produced a double spiral structure, corresponding to the rotating quadrupole associated to two co-rotative vortices, which agreed with the literature on the vortex pairing aeroacoustics. Some different behaviors of the acoustic field can also be observed for this pairing geometry.*

keywords: *Aeroacoustics, Vortex pairing, Hydrodynamic instability, Mixing layer, DNS*

1. Introduction

Flow generated sound is a serious problem in many engineering applications. It can cause human discomfort; it affects the stealth operation of military vehicles; etc. Due to the current aircraft traffic, community noise concerns at busy airports constraint the operation of noisy aircraft. In response to this fact, FAA also included stringent regulations to the aircraft noise level operation and certification [Wang *et al.*, 2006; Colonious and Lele, 2004]. Airframe noise is the major responsible for the sound level of landing aircraft, since the propulsion system is near to the lowest power level. The impact of those mentioned facts on the worldwide aircraft industry is the greater attention paid to noise in the design stage, leading to the need of an efficient noise level prediction method.

Hydrodynamic instability phenomena are determinant to a wide family of aerodynamically generated sound. This strong link is due to the transient and periodic nature of both the Hydrodynamic instability and the aerodynamic sound generation phenomena. Two classical cases of aerodynamic sound generation are the vortex-shedding and vortex pairing [Wang *et al.*, 2006; Colonious and Lele, 2004]. The vortex pairing phenomenon follows a chain of events starting with the primary disturbance amplification leading to the production of vortex structures, which is the classical Kelvin Helmholz instability mechanism. Those small primary disturbances exponentially grow in time or space and reach the saturation point, when the vortex structures are formed. Thus, when the vortex distribution geometry is already established, the secondary instability takes place leading to the pairing of the primary vortices. Those steps are better explained in the following sections.

Vortex pairing is a remarkable phenomenon that generates noise in the jet flow case [Colonious *et al.*, 1997; Colonious and Lele, 2004; Wang *et al.*, 2006]. In Colonious *et al.*, 1997 an investigation of the sound radiation in a mixing layer under spatial development was performed. Their work used one fundamental frequency disturbance and its three subharmonic frequencies ($f/2$,$f/4$ and $f/8$) which would lead to three pairings. Once

a shorter streamwise domain was adopted, only two pairings were observed. Direct Numerical Simulation (DNS) results filtered with the pairing frequency and subsequent comparison with the results obtained with the Lilley's acoustic analogy (using DNS data to compute the source terms) were shown. Colonius, et. al. concluded, for the free shear layer problem, that acoustic sources are better modeled by modulated wave packets in the streamwise direction than by the Lighthill's compact quadrupole acoustic sources.

A double spiral structure, corresponding to the rotation of a quadrupole source type was obtained by Large Eddy Simulations (LES) of a free shear layer under spatial development in Bogey *et al.*, 2000. Bogey, et. al. attributed this rotation of the quadrupoles sources to the rollup of the two co-rotative vortices, i.e., the rotation of the vortex structures during the pairing. By comparing the wave pattern generated by the rotation of two close rigid objects on a deep-water surface, one can find analogous to those structures reported in Bogey *et al.*, 2000. This analogy can be done due to the vortex structure momentum, since during the pairing begining there is no much mixture between the two vortices.

In numerical simulations of sound generation, Colonious and Lele, 2004; Colonious *et al.*, 1997 showed typical discrepancies between the disturbances near the vortical region and the acoustic disturbances at the far field region of 4 or even 5 orders of magnitude lower. This shows that, the code accuracy is strongly relevant for aeroacoustic study purposes. A code developed by Germanos and Medeiros, 2005 was used to investigate the flow instability of a compressible shear layer. The code accuracy was an important concern in their work. They used a high order compact finite difference scheme for computing the spatial derivatives and a 4^{th} order Runge-Kutta scheme for the time integration. Germanos and Medeiros, 2005 verified the code against the Linear Stability Theory (LST).

The current work presents the tests performed to validate and verify the code used to investigate the vortex pairing aeroacoustics. The strategy adopted in this code was the DNS with a 6^{th} order compact finite difference scheme, proposed by Lele, 1992. A 4^{th} order Runge Kutta integration scheme was also used in this code. The same code developed by Germanos and Medeiros, 2005 was used with a different formulation. The formulation adopted was proposed by Sesterhenn, 2001.

In the present work, the pairing simulations were performed under temporal development. The domain used for the simulations was large enough to capture the acoustic far field. Qualitative acoustic source characterization, such as the directivity and the acoustic structures caused by a single pairing, could be done with the simulation results. The aim of this analysis is to investigate the sound source features found by Colonious *et al.*, 1997 and Bogey *et al.*, 2000. Apparently, the time development of a single pairing in a wide domain has not been reported previously in the literature. Once we characterize the acoustic source of sound of a single pairing it can become easier to understand more complex cases, such as a shear layer under spatial development with more than one pairing.

2. Linear stability theory

The aim of this section is to show the results of a verification test with comparisons with the LST prediction. The case study is the Kelvin-Helmholz instability in a temporal development of a 2D free shear layer problem. The LST predicts the time amplification of eigenfunctions for a time constant base-flow. To keep a constant base-flow in time, a source term was used for the x-direction momentum equation in such a way that no viscous enlargement occurred in time. A $0 < x < 7; -14 < y < 14$ domain was adopted with 32 points along the x-direction and 128 points along the y-direction. Periodic boundary conditions for the x-direction and the free-slip boundary condition for the y-direction were used. A similar validation methodology was employed by Fortuné, 2000. The base-flow can be viewed in Fig. 1.

The problem set-up is:

$$\delta_w = 1; \qquad c_{ref} = 340.21 \qquad Ma = 0.05; \qquad U_{max} = Mac_{ref};$$

$$u(x, y, t = 0) = U_{max} \tanh\left(\frac{2y}{\delta_w}\right) + u_p(x, y); \qquad v(x, y, t = 0) = v_p(x, y);$$

$$Re = \frac{\rho U_{max} \delta_w}{\mu} = 80;$$

where: δ_w is the mixing layer vorticity thickness; c_{ref} is the reference speed of sound; Ma is the local Mach number on the upper free stream; $u_p(x, y)$ and $v_p(x, y)$ are disturbances of the velocity components in x and y directions, respectively. For the nondimensionalization, the reference scale is δ_w, the reference velocity is U_{max}, time is non-dimensionalized by $\frac{\delta_w}{U_{max}}$, entropy by c_p, density by the reference density (ρ_{ref}), temperature by $T_{ref} = \frac{c_{ref}^2}{\gamma R}$ and the pressure by the reference dynamic pressure ($\rho_{ref} U_{max}^2$). The disturbance v_p used was:

$$v_p(x, y) = e^{-\sigma\left(\frac{y}{\delta_w}\right)} \left[A_0 \cos\left(\frac{2\pi x}{L_x}\right)\right].$$

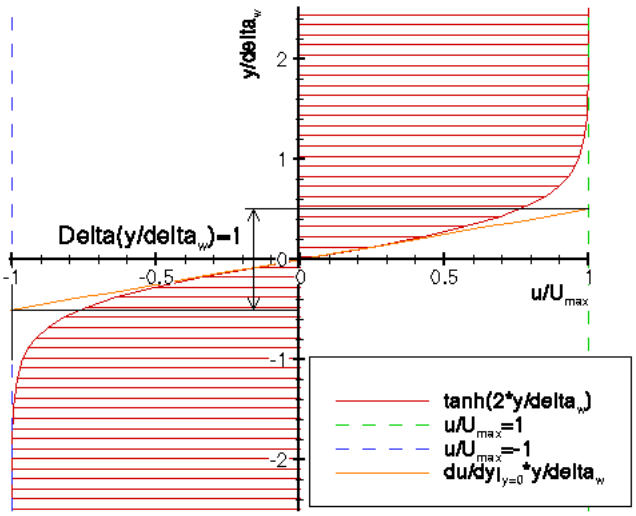

Figure 1: Base-flow sketch of the velocity profile and the δ_w definition.

By assuming the disturbance field as incompressible, i.e., $\frac{\partial u_p}{\partial x} + \frac{\partial v_p}{\partial y} = 0$, an appropriate u_p disturbance field could be obtained.

For this set of parameters defined above, the linear stability theory predicts a amplification rate of 0.31, i.e., any disturbance variable should grow in time as: $e^{0.31t}$. The exponential growth region and the saturation point of the disturbance can be seen in Fig. 2. This figure shows the LST prediction and the simulation result. The CFL number employed in this simulation was 0.55 and the viscous criterion stand beneath 0.002. The time development of the vorticity field obtained from this simulation is showed in the frame sequence of Fig. 3. The saturation point starts near the frame 3(f), i.e., when the vortex takes its recognizable shape.

3. Formulation

The aim of this section is to provide a clear understanding on the fundamentals of the characteristic-type variables proposed by Sesterhenn, 2001. The formulation will adopt the classical notation: ρ, c, p, u, s as the density, speed of sound, pressure, velocity and entropy, respectively.

3.1. Thermodynamic state equation and properties

In the present work we shall assume the thermally ideal gas equation:

$$p = \rho R T. \tag{1}$$

Differentiating equation (1):

$$dp = d\rho RT + \rho R dT. \tag{2}$$

Using the fundamental equation of enthalpy and the thermally ideal gas hypothesis ($dh = c_p dT$) we can write:

$$dh = c_p dT = Tds + \frac{dp}{\rho}. \tag{3}$$

Replacing (dT) and (T) in (3) from the equations (2) and (1), respectively, we obtain:

$$c_p\left(\frac{dp}{\rho R} - \frac{pd\rho}{\rho^2 R}\right) = \frac{p}{\rho R} ds + \frac{dp}{\rho}.$$

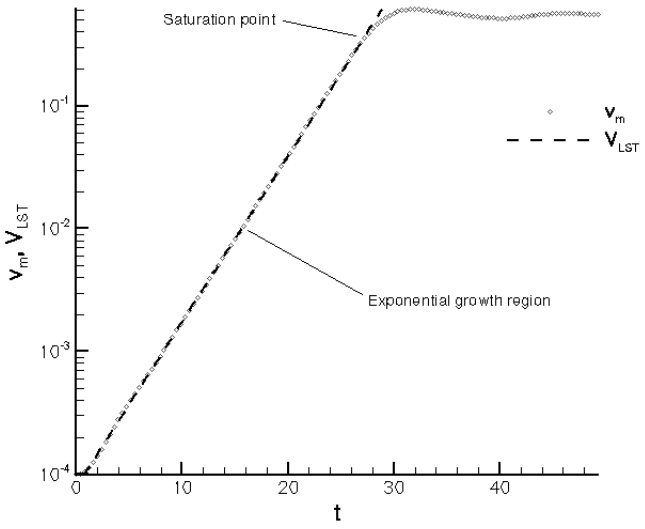

Figure 2: Time development predicted by the simulation and predicted by the LST.

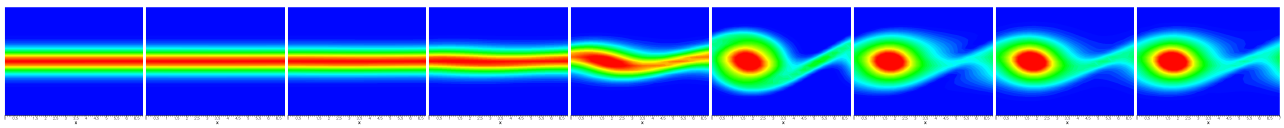

(a) (b) (c) (d) (e) (f) (g) (h) (i)

Figure 3: Time sequence of the vorticity field, the first frame is at $t = 0.0551\frac{\delta_w}{U_{max}}$ the time step between each frame is $\Delta t = 0.174\frac{\delta_w}{U_{max}}$.

Now, using $(R = c_p - c_v)$ and $\left(\gamma = \frac{c_p}{c_v}\right)$ we can write:

$$dp\frac{1}{\gamma - 1} = \frac{p}{R}ds + \frac{\gamma RT}{\gamma - 1}d\rho.$$

Thus, using $\left(c^2 = \gamma RT\right)$ we obtain equation:

$$d\rho = \frac{dp}{c^2} - \frac{p}{c^2 c_v}ds. \tag{4}$$

3.2. 1D Equations of motion

The one dimensional Euler equations of motion for a plane wave, for the reversible case, are:

$$\frac{\partial \rho}{\partial t} + \rho\frac{\partial u}{\partial x} + u\frac{\partial \rho}{\partial x} = 0 \tag{5}$$

$$\rho\left(\frac{\partial u}{\partial t} + u\frac{\partial u}{\partial x}\right) + \frac{\partial p}{\partial x} = 0 \tag{6}$$

$$\frac{\partial s}{\partial t} + u\frac{\partial s}{\partial x} = 0. \tag{7}$$

Again, using the hypothesis of thermally ideal gas, we can now plug Eq. (4) into the term $\partial\rho$ for the continuity equation (5):

$$\frac{\partial p}{\partial t} + u\frac{\partial p}{\partial x} + \rho c^2 \frac{\partial u}{\partial x} - \frac{p}{c_v}\left(\frac{\partial s}{\partial t} + u\frac{\partial p}{\partial x}\right) = 0 \tag{8}$$

$$\rho\left(\frac{\partial u}{\partial t} + u\frac{\partial u}{\partial x}\right) + \frac{\partial p}{\partial x} = 0 \tag{9}$$

$$\frac{\partial s}{\partial t} + u\frac{\partial s}{\partial x} = 0. \tag{10}$$

The entropy equations (7) and (10) assumes that the flow is under a reversible process, i.e., the entropy rate of change for a given point is only caused by the convection of entropy. Likewise, it assumes that there is no viscous dissipation mechanisms and that there is no entropy generation. In fact, the entropy term in the continuity equation (10) could be simplified. However, to provide a wider valid solution we shall keep this term and generic flows, such as irreversible flows, could be simulated by the continuity equation as it stands.

Multiplying the Eq. (8) by $\left(\frac{1}{\rho c}\right)$, adding $\left(\frac{1}{\rho}\right)$ times the Eq. (9), using $\left(c_v = \frac{c_p}{\gamma}\right)$ and $\left(c^2 = \gamma RT\right)$, one can write Eq. (11). Now with analogous operations but instead of adding, subtracting $\left(\frac{1}{\rho}\right)$ times the Eq. (9) we can write Eq. (12):

$$\left(\frac{1}{\rho c}\frac{\partial p}{\partial t} + \frac{\partial u}{\partial t}\right) + (u+c)\left(\frac{1}{\rho c}\frac{\partial p}{\partial x} + \frac{\partial u}{\partial x}\right) - \frac{c}{c_p}\left(\frac{\partial s}{\partial t} + u\frac{\partial s}{\partial x}\right) = 0 \tag{11}$$

$$\left(\frac{1}{\rho c}\frac{\partial p}{\partial t} - \frac{\partial u}{\partial t}\right) + (u-c)\left(\frac{1}{\rho c}\frac{\partial p}{\partial x} - \frac{\partial u}{\partial x}\right) - \frac{c}{c_p}\left(\frac{\partial s}{\partial t} + u\frac{\partial s}{\partial x}\right) = 0 \tag{12}$$

$$\frac{\partial s}{\partial t} + u\frac{\partial s}{\partial x} = 0. \tag{13}$$

Using the fundamental enthalpy equation (3), the differential form of speed of sound $\left(\delta T = \frac{2c}{\gamma R}\delta c\right)$ and the speed of sound definition, the value $\left(\frac{\delta p}{\rho c} \pm \delta u\right)$ can be written in the following form:

$$\frac{\delta p}{\rho c} \pm \delta u = \frac{2}{(\gamma-1)}\delta c \pm \delta u - \frac{c}{\gamma R}\delta s.$$

Using the definition of Riemann variables $\left(\mathfrak{R}^{\pm} = \frac{2}{(\gamma-1)}c \pm u\right)$ we can write Eq. (14):

$$\frac{\delta p}{\rho c} \pm \delta u = \delta\mathfrak{R}^{\pm} - \frac{c}{\gamma R}\delta s. \tag{14}$$

For the case of homentropic flow ($\delta s \equiv 0$), using (14), both the Eq. (11) and Eq. (12) can be written as functions of the Riemann variables:

$$\frac{\partial \mathfrak{R}^{\pm}}{\partial t} + (u \pm c)\frac{\partial \mathfrak{R}^{\pm}}{\partial x} = 0. \tag{15}$$

Eqs. (15) state that the Riemann variables ($\mathfrak{R}^{\pm}$) are conserved along the characteristic paths $\left(\frac{\partial x}{\partial t} = (u \pm c)\right)$ in space and time. Due to this conservation, for homentropic flow, Riemann variables are named Riemann invariants.

Now, defining $X^{\pm}$:

$$\begin{aligned} X^{\pm} &= (u \pm c)\frac{\partial \mathfrak{R}^{\pm}}{\partial x} \\ X^{\pm} &= (u \pm c)\left(\frac{1}{\rho c}\frac{\partial p}{\partial x} \pm \frac{\partial u}{\partial x}\right); \end{aligned} \tag{16}$$

$X^{\pm}$ represents the ($\mathfrak{R}^{\pm}$) rate of change in time. Observe that Eq. (15) traduces the conservation of the quantity ($\mathfrak{R}^{\pm}$) traveling with the relative speed of sound ($u \pm c$). Thus, $X^{\pm}$ represents the acoustic wave in the linear analysis. Through this variable one may explicitly handle the acoustic wave propagation phenomena.

Analogous interpretation of the correlations between the $X^{\pm}$ terms and $\mathfrak{R}^{\pm}$ terms for ($\delta s = 0$) along the path $\left(\frac{\partial x}{\partial t} = u\right)$, i.e. $\left(\frac{\partial s}{\partial t} + u\frac{\partial s}{\partial x} = 0\right)$, and for irreversible flow cases $\left(\frac{\partial s}{\partial t} + u\frac{\partial s}{\partial x} = \sigma\right)$ can be seen in Sesterhenn, 2001.

Now, one shall diagonalize the set of Eqs. (8), (9) and (10) by adding and subtracting to the Eq. (8), $\frac{c}{2}$ times the Eq. (9). This operation basically added zero to the continuity equation, but it will enable us to explicitly write the acoustics terms in the continuity equation:

$$\frac{\partial p}{\partial t} + \frac{\rho c}{2}\left[(u+c)\left(\frac{1}{\rho c}\frac{\partial p}{\partial x} + \frac{\partial u}{\partial x}\right) + (u-c)\left(\frac{1}{\rho c}\frac{\partial p}{\partial x} - \frac{\partial u}{\partial x}\right)\right] - \frac{p}{c_v}\left(\frac{\partial s}{\partial t} + u\frac{\partial p}{\partial x}\right) = 0.$$

By performing analogous operation, i.e. adding and subtracting to the Eq. (9) $\frac{1}{\rho c}$ times the Eq. (8), one can write:

$$\frac{\partial u}{\partial t} + \frac{1}{2}\left[(u+c)\left(\frac{1}{\rho c}\frac{\partial p}{\partial x} + \frac{\partial u}{\partial x}\right) - (u-c)\left(\frac{1}{\rho c}\frac{\partial p}{\partial x} - \frac{\partial u}{\partial x}\right)\right] = 0.$$

With the two above equations and defining the entropy wave term as: $X^s = u\frac{\partial s}{\partial x}$, we can write the 1D Euler equations in the wave like form:

$$\frac{\partial p}{\partial t} + \frac{\rho c}{2}\left[X^+ + X^-\right] - \frac{p}{c_v}\left(\frac{\partial s}{\partial t} + X^s\right) = 0 \tag{17}$$

$$\frac{\partial u}{\partial t} + \frac{1}{2}\left[X^+ - X^-\right] = 0 \tag{18}$$

$$\frac{\partial s}{\partial t} + X^s = 0. \tag{19}$$

Algebraically, there is no difference between the set of Eqs. (17), (18) and (19) and the set of Eqs. (5), (6) and (7). But in practice the first set of Eqs., 17, 18 and 19, enable to explicitly handle the wave terms. It makes it easier to introduce the non-reflecting boundary condition.

Now, for illustration and definition purposes, suppose a coordinate system in which the x-axis grows from left to right. For a subsonic flow case: X^+ plane wave will travel towards x-direction, X^- plane wave will travel towards the opposite direction, X^s waves will travel with the same direction as the local velocity (u). This is sketched in the Fig. 4 as a sound wave which travels from left to right (X^+), another sound wave which travels from right to left (X^-) and, for a positive velocity u, an entropy wave which travels from left to right.

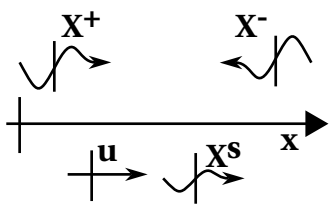

Figure 4: Characteristic-type variables scheme for a subsonic flow.

With this background of the characteristic-type variables for the 1D flow case provided by the present section, we shall present the 3D flow case equations.

3.3. 3D Equations of motion

Three-dimensional formulation can be derived by decomposing the Navier Stokes equations and performing analogous steps given for the 1D formulation for each direction, i.e., diagonalizing the Navier Stokes equations. For brevity, we shall not give details of the necessary steps to obtain the full 3D equations. A detailed characteristic-type formulation of the 3D Navier Stokes equations can be found in Sesterhenn, 2001. The 3D set of equations written in the wave-like form are:

$$\begin{aligned}
\frac{\partial p}{\partial t} &= -\frac{\rho c}{2}\left[\left(X^+ + X^-\right) + \left(Y^+ + Y^-\right) + \left(Z^+ + Z^-\right)\right] + \frac{p}{c_v}\left(\frac{\partial s}{\partial t} + X^s + Y^s + Z^s\right) \\
\frac{\partial u}{\partial t} &= -\left[\frac{1}{2}\left(X^+ - X^-\right) + Y^u + Z^u\right] + \frac{1}{\rho}\frac{\partial \tau_{1j}}{\partial x_j} \\
\frac{\partial v}{\partial t} &= -\left[X^v + \frac{1}{2}\left(Y^+ - Y^-\right) + Z^v\right] + \frac{1}{\rho}\frac{\partial \tau_{2j}}{\partial x_j} \\
\frac{\partial w}{\partial t} &= -\left[X^w + Y^w + \frac{1}{2}\left(Z^+ - Z^-\right)\right] + \frac{1}{\rho}\frac{\partial \tau_{3j}}{\partial x_j} \\
\frac{\partial s}{\partial t} &= -\left(X^s + Y^s + Z^s\right) + \frac{R}{p}\left(-\frac{\partial q_i}{\partial x_i} + \phi\right).
\end{aligned} \tag{20}$$

With the wave terms, heat transfer term, viscous term and viscous dissipation term defined as follows:

$$\begin{aligned}
X^+ = (u+c)\left(\frac{1}{\rho c}\frac{\partial p}{\partial x} + \frac{\partial u}{\partial x}\right); \qquad X^- &= (u-c)\left(\frac{1}{\rho c}\frac{\partial p}{\partial x} - \frac{\partial u}{\partial x}\right); \\
X^v = u\frac{\partial v}{\partial x}; \qquad X^w = u\frac{\partial w}{\partial x}; \qquad X^s &= u\frac{\partial s}{\partial x}; \\
Y^+ = (v+c)\left(\frac{1}{\rho c}\frac{\partial p}{\partial y} + \frac{\partial v}{\partial y}\right); \qquad Y^- &= (v-c)\left(\frac{1}{\rho c}\frac{\partial p}{\partial y} - \frac{\partial v}{\partial y}\right); \\
Y^u = v\frac{\partial u}{\partial y}; \qquad Y^w = v\frac{\partial w}{\partial y}; \qquad Y^s &= v\frac{\partial s}{\partial y}; \\
Z^+ = (w+c)\left(\frac{1}{\rho c}\frac{\partial p}{\partial z} + \frac{\partial w}{\partial z}\right); \qquad Z^- &= (w-c)\left(\frac{1}{\rho c}\frac{\partial p}{\partial z} - \frac{\partial w}{\partial z}\right); \\
Z^u = w\frac{\partial u}{\partial z}; \qquad Z^v = w\frac{\partial v}{\partial z}; \qquad Z^s &= w\frac{\partial s}{\partial z}; \\
\tau_{ij} = \mu\left[\frac{\partial u_j}{\partial x_i} + \frac{\partial u_i}{\partial x_j} - \frac{2}{3}\left(\nabla\vec{V}\right)\delta_{ij}\right]; \\
q_i = -\lambda\frac{\partial T}{\partial x_i}; \\
\phi = \tau i j E_{ij}; \\
E_{ij} = \frac{1}{2}\left(\frac{\partial u_i}{\partial x_j} + \frac{\partial u_j}{\partial x_i}\right).
\end{aligned}$$

Observe that new terms which were not present in the previous formulation (1D flow case) have appeared in the 3D flow case. Those terms are called momentum waves, ${X_i}^{u_j}\left(1-\delta_{ij}\right)$, and represent the injection of x_j-direction momentum due to its gradient in x_i-direction.

A sketch of the acoustic wave terms belonging to the characteristic formulation of the 2D Navier Stokes is showed in Fig. 5.

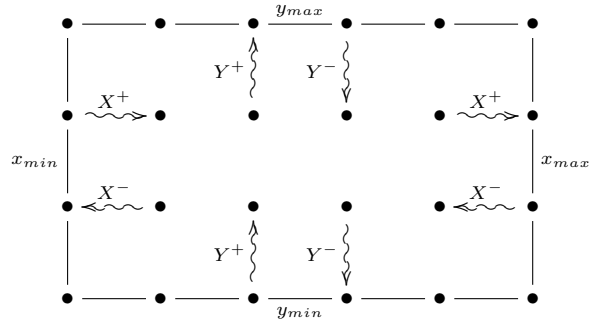

Figure 5: Acoustic wave terms in a two-dimensional domain

4. Anechoic boundary condition test

Non reflecting boundary condition is a challenge for the development of numerical studies in fluid mechanics. Due to the wave like form of the Navier-Stokes equations, the acoustic waves are decomposed into terms with different traveling directions. For the 2D case, the anechoic boundary condition can be implemented in an explicitly way by imposing null incoming waves into the domain. For example, to apply the anechoic boundary condition at the boundary $y = y_{max}$ showed in Fig. 5, it is necessary to impose $Y^- = 0$ along $y = y_{max}$.

The test presented in this section used a Gaussian pressure distribution as the initial condition. The pressure variation amplitude was 10% of that at the far field. The initial entropy field was uniform and the velocities were null. This initial condition could represent a time instant in which two acoustic waves with the same amplitude cross each other. At $y = -0.5$ the anechoic boundary condition was applied, at $y = 0.5$ the rigid boundary condition was applied. Fig. 6 shows the time development of the pressure field. The color scale employed presents from the overall maximum to the minimum pressure.

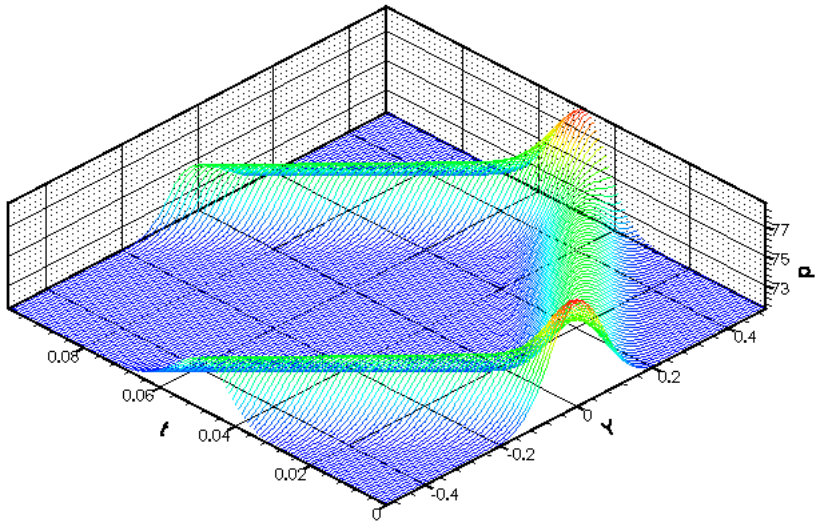

Figure 6: Contour plot of the pressure field development in t and y.

Two tests were performed:

(a) First test case: For a first test, a reflection of 4.5% was obtained in the anechoic boundary. It means that the spurious reflected acoustic wave had an amplitude below 5% of the acoustic wave amplitude outgoing the domain. For this first test, the Neumman boundary condition was used for the pressure ($\frac{\partial p}{\partial y} = 0$), no specified boundary condition was adopted for $\frac{\partial v}{\partial y}$ and it was subsequently computed Y^- and $Y^+ \rightarrow 0$ along $y = -0.5$.

(b) Second test case: For a second test changing the advection scheme, i.e., using none specified boundary condition for both $\frac{\partial v}{\partial y}$ and $\frac{\partial p}{\partial y}$ and subsequently computing Y^- and $Y^+ \rightarrow 0$ along the path $y = -0.5$, it was possible to obtain a reflection rate below 0.08%.

Fig. 7 shows the development of the pressure field $P(y)$ in time t. In Fig. 7(a) the color scale shows the pressure level of the spurious reflection obtained by the technique used in test (a). In Fig. 7(b) the same is

done for test (b) but the color scale is different to indicate the reflected wave. Through those two Figs. it is possible to observe the different reflection amplitude obtained by tests (a) and (b).

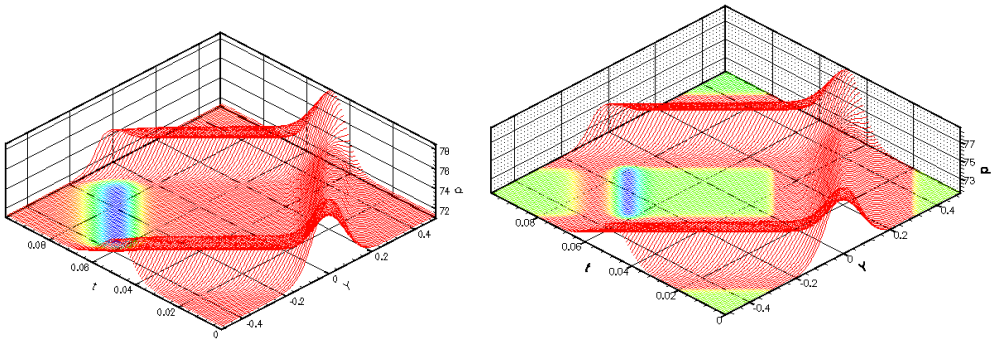

(a) First test case (b) Second test case

Figure 7: Color scale ranging the pressure field caused by spurious reflection for cases (a) and (b). The scales ranges from blue color (lowest reflected pressure level) to red color (highest reflected pressure level).

4.1. Anechoic boundary condition conclusion

By changing the advection scheme, a reflection factor reduction of more than 50 was observed. Test (a) was possibly overconstrained. The imposition of $Y^+ = 0$ along $y = -0.5$ is one constraint which implicitly states a relationship between $\frac{\partial v}{\partial y}$ and $\frac{\partial p}{\partial y}$ during the simulation. Likewise, for a pure sound wave propagation case, it is better to assume neither $\frac{\partial v}{\partial y} = 0$ nor $\frac{\partial p}{\partial y} = 0$.

It is important to emphasize that the only technique used to mimic the anechoic boundary condition employed for both simulations was the imposition $Y^+ = 0$ along $y = -0.5$. By using other techniques, such as *buffer zones* and gradual acceleration of the sound speed near the boundary with the technique employed for both simulations an even lower spurious reflection can be obtained.

5. Free Shear Layer

Different initial conditions were tested aimed at reproduce the acoustic field caused by a single pairing. By the first technique used to generate the disturbance field presented in section 5.1, spurious acoustic waves were created at the initial condition. Due to the periodic boundary conditions adopted for the x-direction, those waves were present during all the simulation time. It eventually presented sound waves with amplitudes equal or higher than those produced by the vortex pairing. With initial disturbances compounded by wave packets no spurious acoustic waves were created at the initial conditions.

5.1. Initial conditions

For the present and following sections, the same non-dimensional scheme of section 2 is used. For the free shear layer problem the initial condition adopts a parallel base-flow with a temperature profile proposed by Crocco-Busemman, Fortuné, 2000. The initial velocity field takes the form: $u(x,y) = \tanh\left(\frac{2y}{\delta_w}\right) + u_p(x,y)$ and $v(x,y) = 0 + v_p(x,y)$. In which $u_p(x,y)$ and $v_p(x,y)$ are small disturbances of the flow. The performed simulations had a disturbance level of:

$$max\left[\frac{max\left[u_p(x,y)\right]}{U_{max}}; \frac{max\left[v_p(x,y)\right]}{U_{max}}\right] < 10^{-5}$$

.

A number of tests were done aiming at the production of a single vortex pairing in a wide domain. In one of them, the disturbance field:

$$u_p(x,y) = 2\frac{\sigma y}{\delta_w}e^{-\sigma\left(\frac{y^2}{\delta_w}\right)}\frac{L_x}{2\pi}\left[A_0\sin\left(\frac{2\pi x}{L_x}\right)+\frac{A_1}{2}\sin\left(\frac{4\pi x}{L_x}\right)\right]; \quad (21)$$

$$v_p(x,y) = e^{-\sigma\left(\frac{y^2}{\delta_w}\right)}\left[A_0\cos\left(\frac{2\pi x}{L_x}\right)+A_1\cos\left(\frac{4\pi x}{L_x}\right)\right]; \quad (22)$$

was multiplied by a windowing function obtained from the combination of two hyperbolic tangent functions:

$$f_w(x,y) = \frac{\tanh\left[k\left(x-x_0\right)\right]+\tanh\left[k\left(x_1-x\right)\right]}{2}.$$

Once the disturbance field was multiplied by the windowing function, $\frac{\partial\rho}{\partial t}$ assumed non-zero values for the whole domain at the initial condition and spurious acoustic waves created at the initial condition disallowed the clear observation of the pairing acoustic field.

5.1.1. Complex wave packets

This technique was used by Medeiros, 1996 to study the nonlinear behavior of modulated Tollmien-Schlichting waves. This technique is capable of almost-punctually disturb the flow near a given point. The disturbance contains a wide range of frequencies. Aiming at investigate the growth of Tollmien-Schlichting waves created by a wider range of frequencies, Medeiros, 1996 used this technique. To understand this methodology, a disturbance field generated by a single complex wave packet is described below:

$$u_p(x,y) = 2\frac{\sigma y}{\delta_w}e^{-\sigma\left(\frac{y^2}{\delta_w}\right)}A\Re\left[e^{\imath\phi}\left(\sum_{n=1}^{n_{max}}\frac{e^{\imath\frac{2n\pi(x-x_p)}{L_x}}}{\imath\frac{2\pi n}{L_x}}\right)\right]; \quad (23)$$

$$v_p(x,y) = e^{-\sigma\left(\frac{y^2}{\delta_w}\right)}A\Re\left[e^{\imath\phi}\left(\sum_{n=1}^{n_{max}}e^{\imath\frac{2n\pi(x-x_p)}{L_x}}\right)\right]. \quad (24)$$

where x_p is the x coordinate where the disturbances are concentrated. A Gaussian y-profile multiply the wave packet making the disturbances active only in the free shear layer vortical region. Depending on the phase angle ϕ, different disturbance shapes, but with an identical amplitude envelope, are formed at the point x_p.

It is possible to verify that this disturbance field satisfy the mass conservation law for an incompressible flow. By substituting Eqs. (23) and (24) into the mass conservation equation:

$$\frac{\partial u_p}{\partial x}+\frac{\partial v_p}{\partial y} = 2\frac{\sigma y}{\delta_w}e^{-\sigma\left(\frac{y^2}{\delta_w}\right)}A\Re\left[e^{\imath\phi}\left(\sum_{n=1}^{n_{max}}\frac{\imath\frac{2n\pi}{L_x}e^{\imath\frac{2n\pi(x-x_p)}{L_x}}}{\imath\frac{2n\pi}{L_x}}\right)\right]-2\frac{\sigma y}{\delta_w}e^{-\sigma\left(\frac{y^2}{\delta_w}\right)}A\Re\left[e^{\imath\phi}\left(\sum_{n=1}^{n_{max}}e^{\imath\frac{2n\pi(x-x_p)}{L_x}}\right)\right];$$

$$\Rightarrow \frac{\partial u_p}{\partial x}+\frac{\partial v_p}{\partial y} = 2\frac{\sigma y}{\delta_w}e^{-\sigma\left(\frac{y^2}{\delta_w}\right)}A\Re\left[e^{\imath\phi}\left(\sum_{n=1}^{n_{max}}e^{\imath\frac{2n\pi(x-x_p)}{L_x}}\right)\right]-2\frac{\sigma y}{\delta_w}e^{-\sigma\left(\frac{y^2}{\delta_w}\right)}A\Re\left[e^{\imath\phi}\left(\sum_{n=1}^{n_{max}}e^{\imath\frac{2n\pi(x-x_p)}{L_x}}\right)\right];$$

$$\Rightarrow \frac{\partial u_p}{\partial x}+\frac{\partial v_p}{\partial y} = 0.$$

It means that the incompressible disturbance field hypothesis is satisfied and no spurious acoustic waves are created at the initial condition.

For illustration purposes, we define a domain $0 \leq x \leq L_x = 150$ and $-200 \leq y \leq 200$ and one point $x_p = 75$. Figs. 8 shows the contour plots of the vorticity field with a vector plot of the local velocity disturbance compounded by Eqs. 23 and 23 for different ϕ values inside the previously defined domain. These figures uses a strong zoom near the point $x = x_p = 75; y = 0$. It is possible to observe that:

(a) For $\phi = \frac{-\pi}{2}$ an anti-clockwise rotating vortex is found at $(x_p, 0)$ (Fig. **??**);

(b) For $\phi = 0$ two counter-rotating vortices are found at $(x_p, 0)$ (Fig. **??**);

(c) For $\phi = \frac{\pi}{2}$ an clockwise rotating vortex is found at $(x_p, 0)$(Fig. **??**);

(d) For $\phi = \pi$ two counter-rotating vortices are found at $(x_p, 0)$(Fig. **??**).

Some of those wave-packets shown in Fig.8 will be used to compound the final disturbance necessary to reproduce a single vortex pairing inside a wide domain.

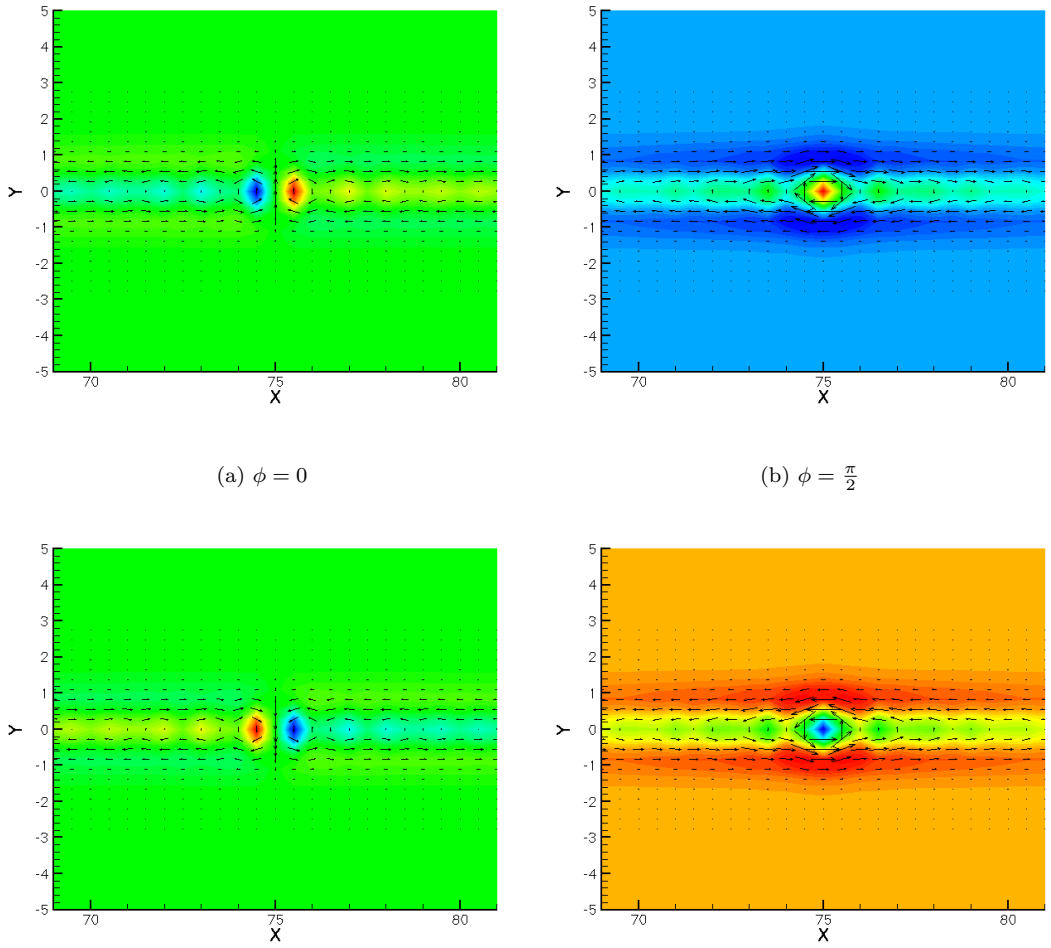

(a) $\phi = 0$ (b) $\phi = \frac{\pi}{2}$

(c) $\phi = \pi$ (d) $\phi = \frac{3\pi}{2}$

Figure 8: Contourplot of vorticity disturbance and vector plot of local velocity disturbance produced by wave packets with $x_p = 75$ and with different phase angle ϕ. Some of those disturbances will be united to compound the final disturbance field used to generate a single vortex pairing inside a wide domain.

5.2. Results

The domain adopted for the present formulation is $0 \leq x \leq L_x = 300$ and $-150 \leq y \leq 150$. The mesh used for this case was uniformely distributed along x-direction with $\delta x = 0.6$ and the y distribution was slightly stretched with a expansion factor of 1.1 and 600 points. For non-aliasing the disturbances, a cut off wavenumber of $n_{max} = 80$ was adopted. 4 different wave packets were used to generate the initial disturbance field. Each one of these 4 wave packet was composed by 80 different wavelengths. The 4 employed wave packets are shown below:

(a) Eqs. 23 and 24 with $\phi = \frac{\pi}{2}$ and $x_p = 145.75$;

(b) Eqs. 23 and 24 with $\phi = 0$ and $x_p = 145$;

(c) Eqs. 23 and 24 with $\phi = \frac{\pi}{2}$ and $x_p = 154.25$;

(d) Eqs. 23 and 24 with $\phi = \pi$ and $x_p = 155$;

(a) and (b) wave packets were concentrated in $x \approx 146$; $y = 0$;(c) and (d) wave packets were concentrated in $x \approx 154$; $y = 0$.

The disturbances nuclei $x \approx 146$ and $x \approx 154$ had equal magnitude, i.e., a constant value of A was used for each one of the wave packets presented in 5.2. The disturbances did not reached $max[u_p(x,y)/U_{max}; v_p(x,y)/U_{max}] > 10^{-2}$. During the simulation an odd symmetry around the axis defined by $x = L_x/2$ and $y = 0$ was found. The frame sequence of Fig. 9 shows the contour plot of vorticity field along the temporal development of the vortex pairing. It is possible to observe that the vortex pairing occurs near the point $x \approx L_x/2 = 150$; $y = 0$, i.e., at the center of the domain.

Fig. 10 shows the contour plots of the dilatation ($\frac{\partial \rho}{\partial t}$). 40 uniformly varying levels are shown between $-3 \cdot 10^{-5}$ and $3 \cdot 10^{-5}$. The white region of each frame has a vorticity level above 0.1. Through this region it is possible to observe the vortex shape dynamics. With the long x-domain, the effect of the x-direction periodic boundary condition is not clearly observed on the acoustic field presented in Fig. 10. Through the Fig. 10, it is possible to observe the double spiral found by Bogey *et al.*, 2000.

6. Conclusion

In the present work, a brief overview of the verification of a code used to simulate a vortex pairing aeroacoustics is done against the LST results. Tests of the anechoic boundary condition were done aimed at reducing the spurious reflection at the boundaries.

The usage of a disturbance field compounded by modulated wave packets was shown as a efficient way to generate a single vortex pairing inside a wide x-domain of a shear layer flow under temporal development. The results of a single vortex pairing aeroacoustics in a shear layer under temporal development with a large x-domain are presented in section 5.2. For this case it was possible to observe and interpret the acoustic structure patterns generated by the pairing as a double spiral, according to the previous results reported by Bogey *et al.*, 2000. Due to the usage of a low wavenumber cut off, secondary vortices stabilize in a short time period. Only the begining of the pairing could be isolated.

The acoustic field generated by the pairing was found to be some scales larger than the vortices structures on the pairing. A typical size of the vortices reproduced in the presented simulations is about $\frac{L_E}{\delta_w} = 4$ and a $\frac{L_x}{\delta_w} = 300$ x-domain was enough to capture the acoustic structures generated by the vortex pairing.

7. Acknowledgments

We greatly acknowledge the financial support of CAPES and FAPESP. We thanks Prof. Dr. Marcio T. Mendonça and Prof. Dr. Jörn Sesterhenn for the fruitful discussions.

8. Author rights

Authors are the sole responsible for the contents of their papers.

9. References

Bogey, C., Bailly, C., and Juvé, D., 2000, Numerical simulation of sound generated by vortex pairing in a mixing layer, "AIAA Journal", Vol. 12, pp. 2210–2218.

Colonious, T. and Lele, S. . K., 2004, Computacional aeroacoustics: progress on nonlinear problems of sound genereation, "Progress in Aerospace Sciences", Vol. 40, pp. 345–416.

Colonious, T., Lele, S. S. K., and Moin, P., 1997, Sound generation in a mixing layer, "J. Fluid Mech.", Vol. 330, pp. 375–409.

Fortuné, V., 2000, "Étude par Simulation Numérique Directe du rayonnement acoustique de couches de mélabge isothermes et anisothermes", PhD thesis, Université de Poitier.

Germanos, R. A. C. and Medeiros, M. A. F., 2005, Development of a code for a direct numerical simulation of compressible shear flow instabilities, "Congresso Brasileiro de Engenharia Mecânica - COBEM 2005". ABCM, In CD-ROM.

Lele, S. K., 1992, Compact finite difference schemes with spectral-like resolution, "J. Comp. Phys.", Vol. 103, pp. 16–42.

Medeiros, M. A. F., 1996, "The nonlinear behaviour of modulated Tollmien-Schlichting waves", PhD thesis, Cambridge University - UK.

Sesterhenn, J., 2001, A Chracteristic-type formulation of the Navier-Stokes equations for high order upwind schemes, "Computers and Fluids", Vol. **30**, pp. 37–67.

Wang, M., Freund, J. B., and Lele, S. K., 2006, Computational Prediction of Flow-Generated Sound, "Annu. Rev. Fluid Mech.", Vol. 38, pp. 483–512.

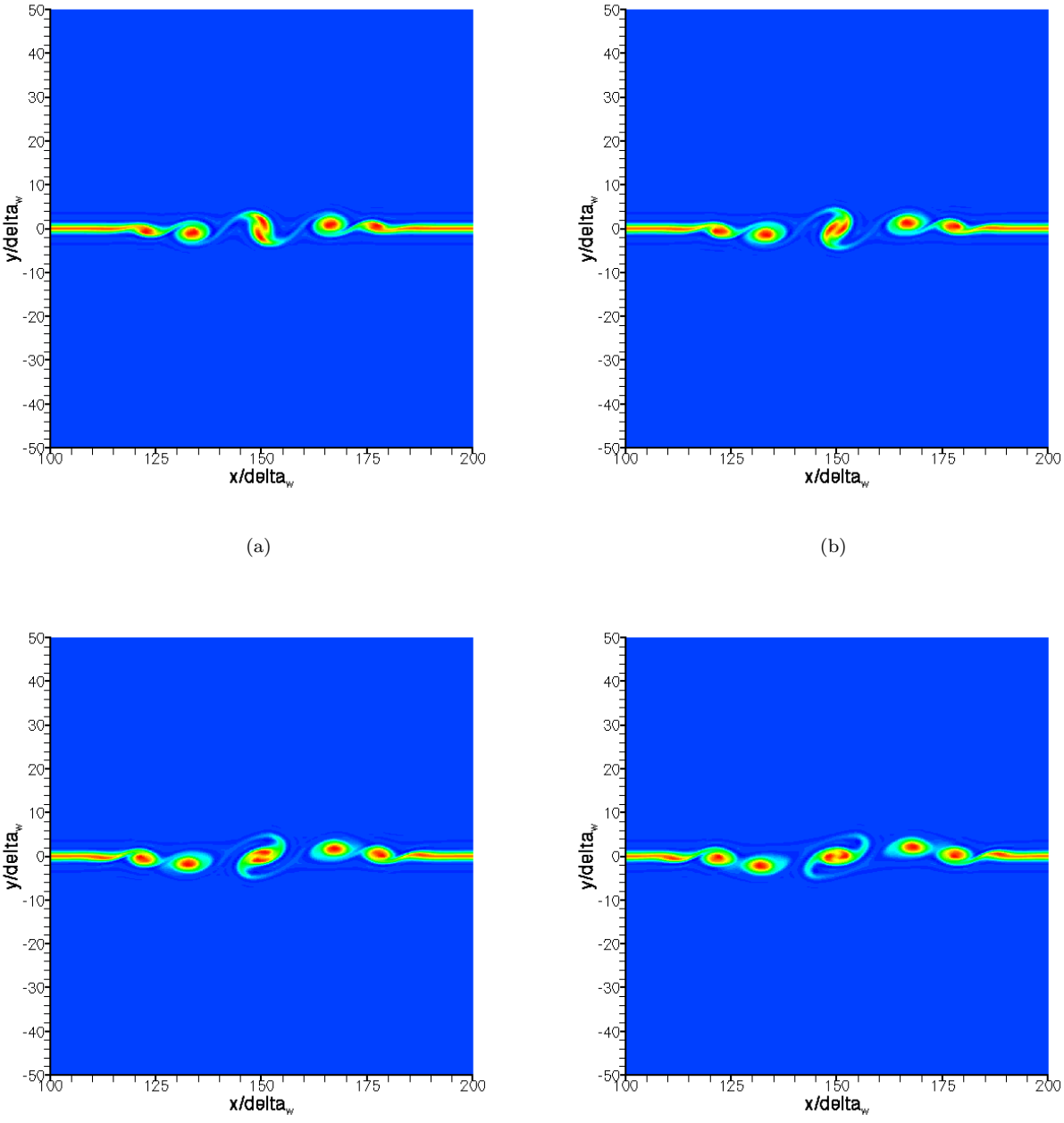

(a) (b)

(c) (d)

Figure 9: Time development of the vorticity field during the pairing.

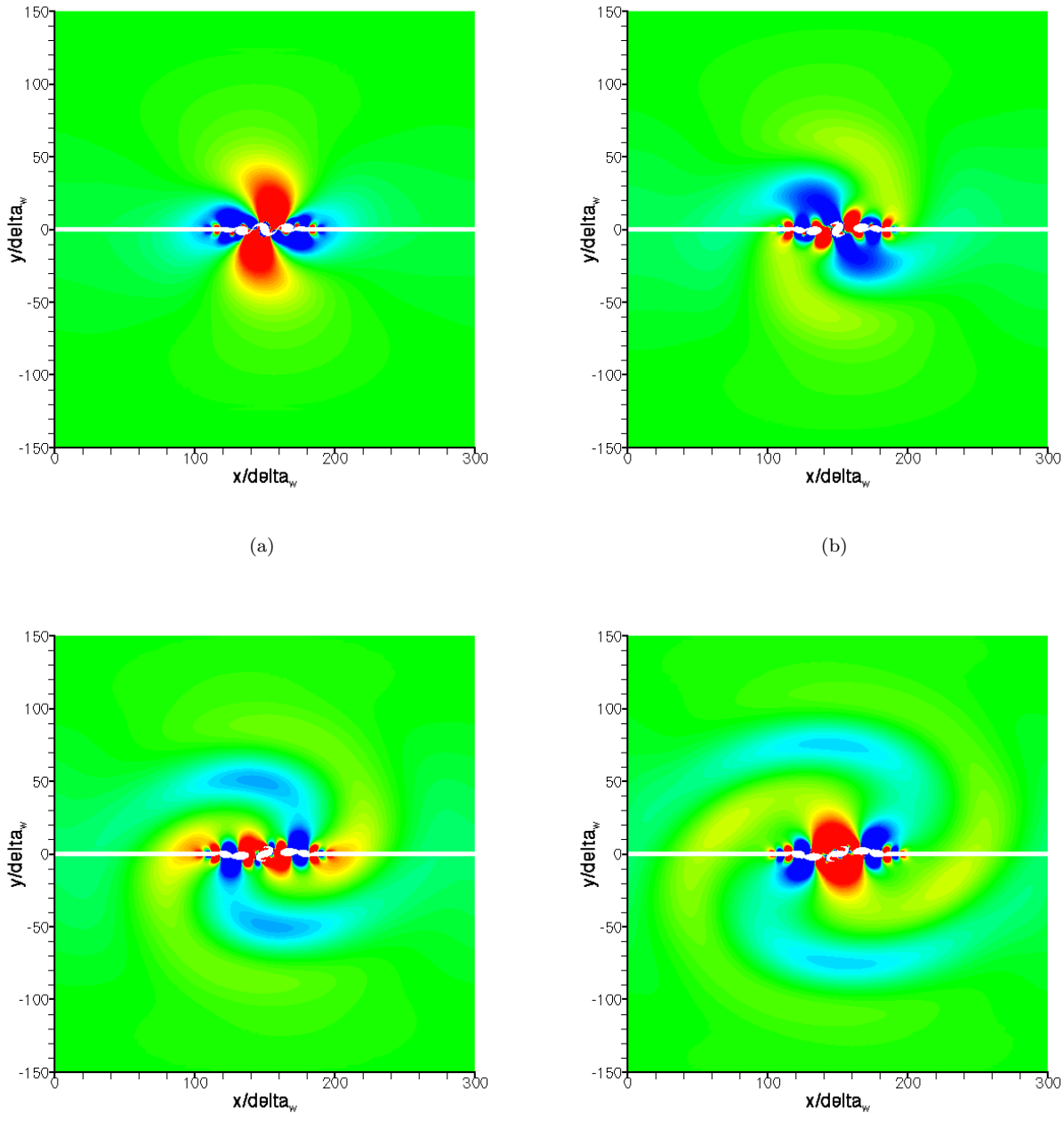

(a) (b)

(c) (d)

Figure 10: Temporal development of the dilatation field ($\frac{\partial \rho}{\partial t}$) during the pairing.